Proceedings of the Fifteenth International Conference on
Computational Structures Technology
Edited by: P. Iványi, J. Kruis and B.H.V. Topping
Civil-Comp Conferences, Volume 9, Paper 2.4
Civil-Comp Press, Edinburgh, United Kingdom, 2024
ISSN: 2753-3239, doi: 10.4203/ccc.9.2.4

Correlating Porosity and Photodiode Response in LPBF Manufactured Samples using Spatial Statistics

T. Wilkinson[1], C. Churchman[2], D. Beer[2], B. Koe[2] and D. Barba[1]

[1] E.T.S de Ingeniería Aeronáutica y del Espacio, Universidad Politécnica de Madrid, Spain
[2] Alloyed Ltd, Alloyed Ltd, Yarnton, United Kingdom

Abstract

The detection of porosity within laser powder bed fusion (LPBF) manufactured components is, and always will be an important step for quality assurance and certification. Computed tomography is the gold standard for non-destructive inspection, but the time, monetary investment, and data-handling challenges can be prohibitive, especially for larger components. The utilisation of various in-situ monitoring sensors might prove to be a fast, and cost-effective method for detecting porosity within laser powder bed fusion printed parts but further work is needed to correlate the response of these sensors with different types of defects that appear during the laser powder bed fusion process. In this work, photodiode data collected during the printing of a coupon with a thermal constriction is voxelised into an efficient format, and then the standard deviation of the data contained within each voxel is calculated to provide a measure of the process stability in 3D space. This spatial standard deviation is then shown to correlate well with pores identified using a high-resolution computed tomography scan of the coupon, showing that photodiode data can be used for the detection of certain types of porosity in laser powder bed fusion printed parts.

Keywords: additive manufacturing, laser powder bed fusion, process monitoring, photodiode, computed tomography, porosity

1 Introduction

Laser powder bed fusion is increasingly being deployed in production environments across different sectors, from aerospace and automotive to biomedical. The layer-by-layer manufacturing process offers unprecedented design flexibility, enabling the production of lighter, more efficient heat exchangers, structural components, and hydraulic manifolds using methods such as lattice structures [1] or topology optimisation [2]. Not only does laser powder bed fusion bring design flexibility, but also point-by-point control of the laser. This allows process engineers to control the laser parameters at any point within a structure, enabling a variation of the processing parameters influenced by geometry, simulations, or observed defects.

The validation and certification process of additively manufactured components varies between different sectors and the safety criticality of the component. What is common amongst different validation procedures and in research efforts, in general, is knowledge of the quality of the solidified material within the component. Typically, porosity is used as the first quality metric to determine the success of a given parameter set, and a high density is usually required. The acceptable level of porosity will vary depending on the specific requirements, but for structural components, the goal porosity is generally below 1%. During initial material printing trials and parameter development, a large number of samples are printed, and then destructively tested to determine the resulting porosity using cross-sections and micrograph analysis. For small samples, this approach has proven to be very successful, and widely considered to be standard practice. However, once the samples increase in size, and the testing moves to component-level trials, this approach may not be possible.

Using a CT scanner is a better approach to determining porosity in a larger-scale component. There are many examples of the use of CT within additive manufacturing and a review of the use of micro-CT can be found in the work of Du Plessis et al. [3]. This review explains in detail the key applications of the technology to tasks such as porosity and defect analysis, density measurement, and surface roughness characterisation. However, a CT scanner requires significant investment in terms of acquiring the hardware, providing adequate radiation protection, training operators, and data storage. These factors can prohibit detailed component analysis in a production environment, where minimising cost and analysis time is key to rapid innovation. Moreover, CT scanning is not feasible for certain materials. The quality and contrast of the final CT image are highly sensitive to the material's x-ray attenuation [4], and lower Z metals give poor contrast, whereas high Z materials introduce artefacts. Many research articles document the successful CT scanning of commonly printed alloys such as aluminium [5] and titanium [6]. In both of these projects, the printed samples are relatively small. For larger components, the scan time may extend to multiple hours for a high-resolution image capable of identifying pores [3]. For more exotic materi-

als, such as platinum, the material properties and required scanning time prohibit the use of CT.

Finally, there is in-process monitoring. This refers to the use of various sensors to capture information about the manufacturing process while it is happening. Examples of different technologies that have been used to capture information from an LPBF machine include short-wave infrared (SWIR) imaging [7, 8], off-axis high-speed optical cameras [9], on-axis high-speed optical cameras [10], acoustic sensors [11], and on-axis pyrometry [12]. All of these technologies allow for some level of insight into the formation of the component during its manufacture, which may prove sufficient to predict relevant defect formation without the use of CT scanning. This work will use in-process sensors, namely photodiodes, to identify regions with higher concentrations of defects. within a manufactured component.

2 Methodology

2.1 Printing

The sample geometry was printed in standard AlSi10Mg powder using a Renishaw AM500Q laser powder bed fusion system. The machine was equipped with a dual on-axis photodiode system with a sampling frequency of 100KHz. The two photodiodes capture a range of wavelengths, one capturing the near-infrared range from 700-1040nm, and the other capturing the infrared range from 1090-1700nm. The machine has 4 lasers, only 1 of which was used for this sample.

The sample geometry is of an hourglass shape, with a radius that reduces linearly to a constriction, and then expands again linearly. This thermal constriction was designed to trigger differing thermal conditions within each layer due to smaller cross-sections, shorter layer times, shorter laser return times, and lower thermal conductivity of the part in the z-axis. The component was scanned using parameters tuned to achieve high density and productivity. The higher productivity generally means that higher energy density is used, and the melting mode approaches, or crosses into keyhole. The scanning strategy used a standard meandering pattern and the vector angle was tuned such that the laser never scanned parallel to the direction of the gas flow, preventing melt pool emissions from interfering with the laser beam.

2.2 Photodiode data collection

As discussed in Section 2.1, the Renishaw AM500Q system uses a dual, on-axis photodiode module to record the incident light intensity from the melt pool zone across two different wavelength ranges. These photodiodes capture data at a sampling frequency of 100KHz for every layer during the build, both when the laser is activated and deactivated. All data captured during a layer is saved in a binary format. Each photodiode records a single numerical value per sample, the response in millivolts.

Voxel Size (μm)	Voltage (kV)	Current (μA)	Exposure Time (ms)
25	140	370	500

Table 1: Settings used for the CT scanning of the printed sample.

This response is proportional to the incident light intensity from the melt pool zone.

The two photodiodes used in the system contain sensors of different shapes and cover different fields of view. Photodiode 1 (with a wavelength range of 700-1040nm) uses a square sensor and has a 6x6mm square field of view. Photodiode 2 (1090-1700nm) uses a circular sensor and covers a circular area of 2.4mm diameter. The sizes of each field of view mean that each photodiode is not restricted to just the liquid melt pool and will capture incident light from the surrounding area. Therefore the response given by the photodiode can be thought of as an average value for the exposed area. This field of view is important to take into account during the interpretation of the photodiode signal, as the response is not just dependent on the light intensity of the melt pool zone, but also on the surrounding material.

2.3 CT scanning and registration

Once the sample has been printed, it is removed from the build plate using a wire EDM cutter. Next, the sample was scanned using a Phoenix V|tome|X M300 (Waygate Technologies). The settings for the CT scanner are given in Table 1.

Since the scanned mesh and photodiode data have different sources, these must be globally aligned before any useful conclusions can be drawn. Since the machine instructions are derived from the nominal CAD mesh and the photodiode data uses the same coordinate system as the laser scanning system, the photodiode data is already aligned in space. Hence, the CT-scanned meshes must be aligned to the nominal CAD data such that the photodiode data and CT data can be compared.

VGSTUDIO Max (Volume Graphics, Germany) is used to perform an initial best-fit alignment with the nominal CAD, which ensures the scanned data is centred at the world origin, and the upper surface aligns well with the nominal CAD in terms of the z-translation. This best fit is not perfect, however, and some adjustments are made using Rhino/Grasshopper to achieve the best possible alignment. First, a sample of mesh vertices from the upper surface of the scanned surface mesh is selected and used to create a best-fit plane. This can be seen in Figure 1. Next, the normal of this plane is compared with the global unit z vector, to calculate the transformation to align the two. This transformation is then applied to the surface mesh. Next, the lettering on the upper surface of the scanned mesh is aligned with that of the nominal CAD using a rotation about the global unit z-axis. Both of these transformations are then applied to the pore meshes to align them with the surface mesh and nominal CAD.

Now that the CT data is aligned with the machine data, the photodiode data can be

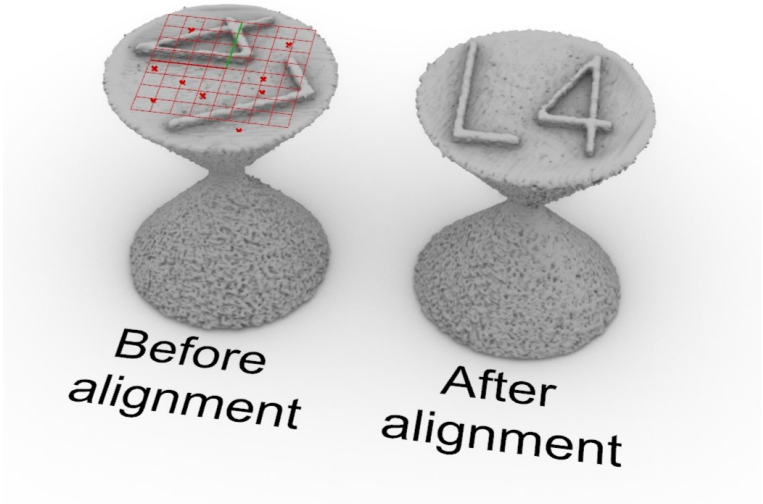

Figure 1: Surface mesh extracted from the CT scan of the printed sample. Also shown is the best-fit plane from the upper surface used to calculate the vertical alignment transformation.

processed.

2.4 Data processing pipeline

This section will detail how the raw data from the laser powder bed fusion machine is processed into a format that is easily visualised and interpreted.

2.4.1 File conversion

As discussed in Section 2.2, the Renishaw AM500Q saves all of the data for each layer into a binary format. For each time interval a range of different metrics are captured, including the world position of the laser, the input power, the activation state, and the millivolt response for each of the two photodiodes. A custom software utility developed by Alloyed (Oxford, UK) was used to extract the laser world position and response signals of the two photodiodes from the binary ".dat" file and convert these into a human-readable ".csv" file for subsequent processing.

2.4.2 Preprocessing

Before performing any statistical analysis, the data passed through 2 key pre-processing steps: downsampling and averaging. The data is down-sampled from 100KHz to 10KHz to reduce the number of data points, then a centred moving average is performed for each layer with a window size of 20 samples. This window was tuned to

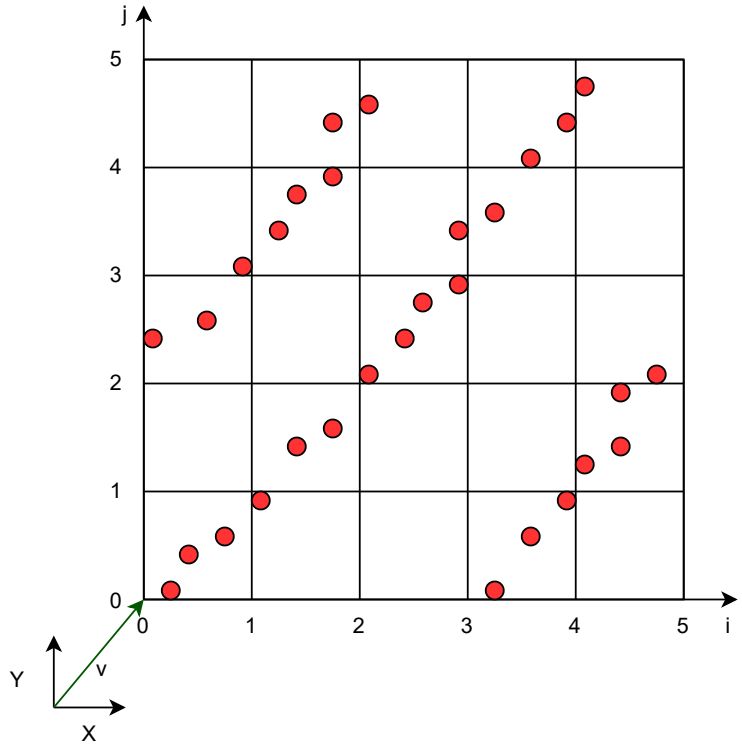

Figure 2: A 2D overview of the voxelisation process used to transform the coordinate data from their global position, P_{xyz} to their corresponding index space position, P_{ijk}. The vector v shows the translation between the global origin and the minimum point of the data's bounding box. This process is extended in 3D.

remove high-frequency noise peaks but allow larger deviations over a longer period to remain.

2.4.3 Voxelisation

Voxelisation is a method of organising the point data into a format that allows for efficient searching, filtering, nearest-neighbour search, and statistical calculations. This process bins each data point into a regular 3D grid of cubic volumes according to their world coordinate, P_xyz, as is highlighted in Figure 2. Each voxel may contain multiple points, depending on the chosen voxel size and the density of points in a given location. The points are stored in a sparse dictionary according to their index space coordinate, P_ijk, for search efficiency. The transformation from world space to index space is a translation and a subsequent integer scaling. This translation applied is the vector from the minimum corner of the data's bounding box to the origin, shown in Figure 2 as V. Next, the points are transformed into index space by dividing their translated coordinate location by the voxel size and rounding down to the next integer

value. This process is defined in equation Equation (1).

$$P_{n,ijk} = Floor(P_{n,xyz}) \tag{1}$$

Each index coordinate is a key in the sparse dictionary, with the corresponding value being the data points within that voxel. In this way, any voxel can be queried using the index space coordinate, and the corresponding sample point data is efficiently found. Constructing the dictionary this way means only voxels containing data are stored.

2.4.4 Statistical Calculation

Organising the point data in a spatial structure means that spatial statistics can be calculated easily and efficiently. For each voxel in index space, a range of statistical measures can be calculated using the photodiode samples contained within, such as the mean, standard deviation, and max. The final calculated values are normalised to be between 0 and 1 according to the maximum and minimum values of each. This normalisation allows for a consistent filtering operation to be applied to select different ranges of values to display. This remapped value can also be mapped to a colour using a colour map for ease of visualisation. For the remainder of this work, we will only focus on the standard deviation.

2.4.5 Implementation

The data reading, voxelisation, and spatial statistics calculations were implemented using a set of custom C# components within Rhino / Grasshopper. In this way, all of the data for the sample could be loaded into the same visual environment; the nominal CAD, the scanned surface, the pores, and the photodiode samples.

3 Results and Discussion

In this section, we will describe the different statistical measures and how they correlate to the appearance of pores according to the CT scan data. First, analysis will be performed on the mesh of pores, and then each of the calculated statistical measures will be discussed and their link to the pore locations will be discussed.

3.1 CT pore mesh analysis

The pores detected using the CT scanner are displayed in Figure 4. 162 pores were identified, and for each, a best-fit sphere was used to characterise the diameter. The mean pore diameter was 78.5μm, and the standard deviation was 13.6μm. The smallest recorded pore was 29.7μm in diameter, and the largest was 123.7μm. The distribution of pore diameters and the distribution of sphericity is shown in Figure 3.

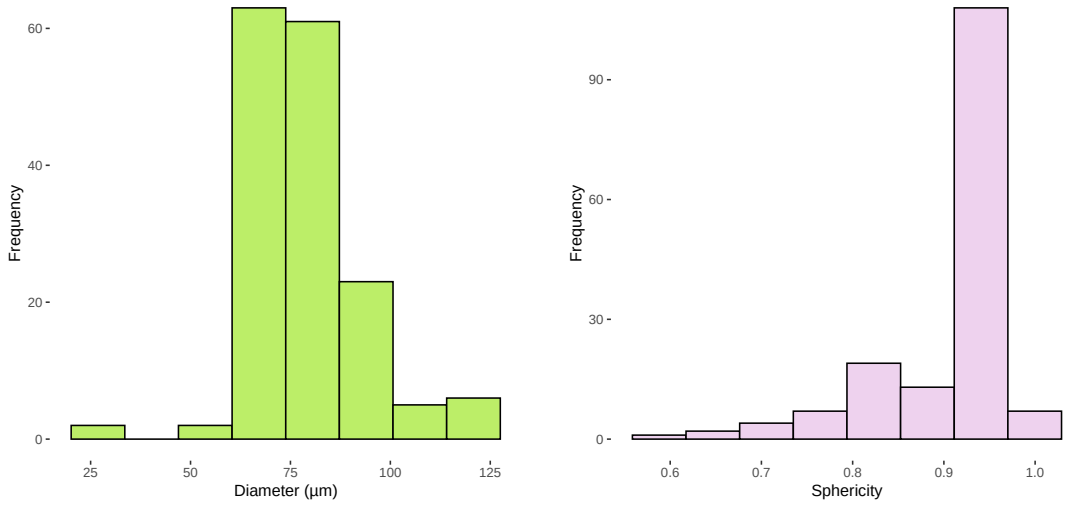

(a) (b)

Figure 3: The distribution of pore diameters (a) and sphericity (b) in the CT scanned mesh.

The number of bins for each histogram was estimated using the Sturges formula. The sphericity, Ψ, was calculated using Equation (2).

$$\Psi = \frac{\pi^{\frac{1}{3}}(6V_p)^{\frac{2}{3}}}{A_p} \tag{2}$$

where V_p and A_p are the volume and surface area respectively of the mesh representing the pore from the CT scan. The sphericity distribution shown in Figure 3(b) suggests that the majority of the pores have a highly spherical shape, meaning that they are likely to be the result of gas bubbles being trapped in the melt pool during solidification. The pores with lower sphericity may result from lack of fusion, or be combinations of multiple pores joining together.

Figure 4 shows that the pores are generally clustered spatially into 2 groups, located on the side of the sample facing into the gas flow direction, in the upper half of the sample. The locations of these two groups correlate with the scanning strategy described in Section 2.1, appearing where the laser changes direction at the start and end of scan vectors. As described in Section 2.1, the scan vectors are chosen such that they are never parallel with the gas flow, and the locations of these groups correspond with the minimum into-gas flow scanning angle chosen for this strategy. This result highlights the importance of selecting an appropriate scanning strategy but also demonstrates that attempting to mitigate one source of defects (scanning into the gas plume and emissions) may lead to other sources (localised porosity due to scan strategy, as shown here).

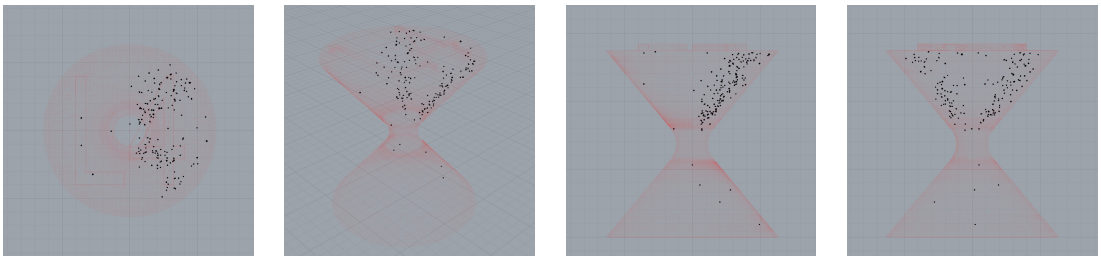

← Gas flow (a) | ↙ Gas flow (b) | ← Gas flow (c) | Gas flow into page (d)

Figure 4: Images showing the spatial distribution of pores (black) identified using the CT scanner with the nominal CAD geometry (red). Images show the (a) top, (b) perspective, (c) front, and (d) side views. The gas flow direction in each image is indicated below.

3.2 Spatial correlation between normalised standard deviation and pore location

For each of the two photodiodes installed on the machine, the data reading, preprocessing, voxelisation, and statistical calculation pipeline are executed, and here we will discuss the outcome. The chosen voxel size was 0.2mm.

The normalised standard deviation of the data contained within each voxel is displayed in Figure 5 for each of the two photodiodes installed in the machine. The number of bins was estimated using the Sturges formula. Both histograms show a large peak in normalised standard deviation in the first bin, corresponding to the voxels where the laser is switched off and travelling between the part and its origin position. This is the only real similarity between the two distributions. The spread of data in Figure 5(a) is much larger than in Figure 5(b). The effect of this on the identification of porous regions will be discussed in the following sections.

3.2.1 Photodiode 1

Figure 5(a) shows the histogram of normalised standard deviation values contained within the voxels using the samples collected by photodiode 1. Excluding the initial large peak in the first bin, there is a single larger peak centred around 0.25, with a tail extending up to 0.80. This larger peak appears to contain two smaller peaks, one from 0.10-0.20, and another from 0.25-0.40.

The peak between 0.10-0.25 contains the voxels located within the bulk of the sample, as well as where the laser is switched off between tracks. We expect the melting process in the core of the component to be the most consistent and have the lowest standard deviation since the laser power, scanning speed, and temperature profiles should be consistent. This is highlighted in Figure 6(a).

The second peak, between 0.25-0.40 normalised standard deviation, corresponds

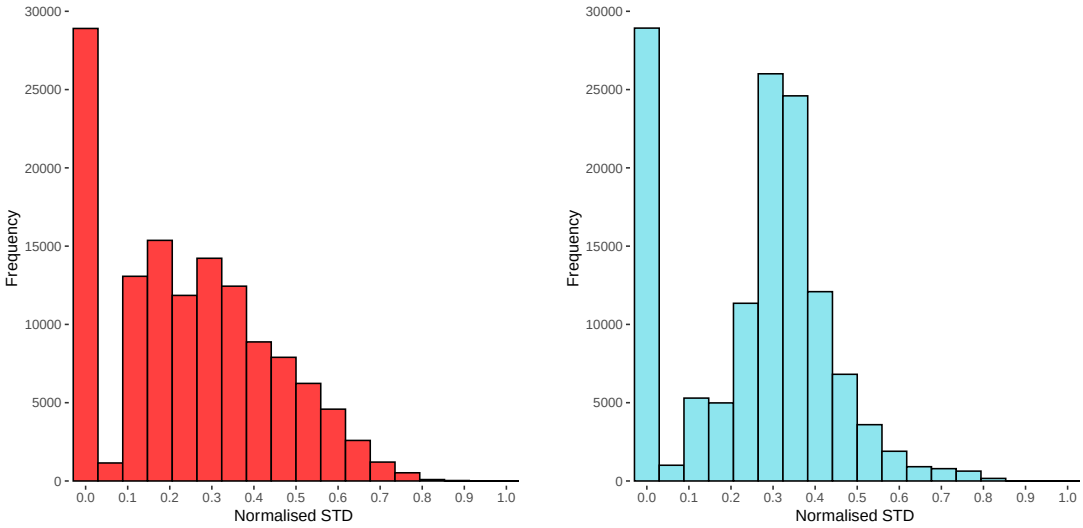

Figure 5: The distribution of the calculated standard deviation per voxel for (a) photodiode 1 and (b) photodiode 2.

to other voxels within the bulk of the material, but also contains voxels close to the transition between the laser switching on and off and the start and end of scan tracks. The 6x6mm square field of view of photodiode 1 likely captures some light emitted from these transition zones, and this will therefore be included in the final response value at a location outside of the transition zone. This region is shown in Figure 6(b). These voxels are similarly located to those within the 0.10-0.25 normalised standard deviation range, but this is to be expected, since the distribution in Figure 5(a) does not show these two peaks as being very distinct. They merge to form a single larger peak.

The voxels with a standard deviation from 0.40-1.00 are shown in Figure 6(c). These voxels almost exclusively contain data located where the laser is physically switching on and off between scan tracks, and this is the cause of the high standard deviation recorded within these voxels. This is where the melting process is the least consistent, and we find that the pores from the CT scan are located in this range.

Filtering the voxels further to a range of normalised standard deviations between 0.65-1.00 reveals the correlation with the porosity observed using the CT scanner. A top-down view of the sample with this filtering is shown in Figure 6(d). In this image, four large clusters of voxels are observed, two of which directly match with the clusters observed in the pore mesh in Figure 4. This leads to the conclusion that pores are more likely to appear where the standard deviation of the voxel data is higher, or the melting process varies more. The other two dense clusters lie directly opposite these and correspond to where the scan vectors start and end. There is no significant porosity in these regions, despite the standard deviation being high. This highlights that standard deviation alone is not a perfect indicator, but it must be considered alongside the gas flow direction to predict the appearance of pores. The remaining voxels

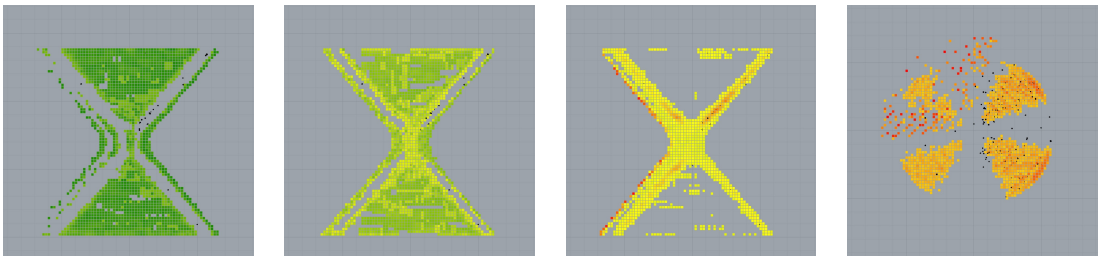

STD: 0.10-0.25 (a) | STD: 0.25-0.40 (b) | STD: 0.40-1.00 (c) | STD: 0.65-1.00 (d)

Figure 6: Images showing 2mm slices through the sample perpendicular to the gas flow direction (a, b, & c) and a top-down view from photodiode 1 filtered within different ranges, given below each image. The colour map goes from green (low normalised standard deviation) to red (high normalised standard deviation).

highlighted in Figure 6(d) correspond to where the laser travels to and from its origin position.

3.2.2 Photodiode 2

Figure 5(b) shows the distribution of normalised standard deviation of photodiode 2 data contained within the voxel grid. Ignoring the initial large peak of values in the first bin, the histogram only contains one significant peak. There is a plateau between 0.10-0.20 normalised standard deviation, corresponding to voxels that lie outside of the scanning area, where the laser is switched off between tracks. The field of view for photodiode 2 is smaller, so there will be less emitted light collected from the material surrounding the melt pool zone, and this is likely the reason for this zone being more well-defined compared to photodiode 1.

The main significant peak spans between 0.2-0.45 normalised standard deviation. The voxels corresponding to this peak are shown in Figure 7(b). This peak encapsulates the bulk of the sample and separates this stable section from the other regions shown in Figure 7. Figure 7(b) shows that the normalised standard deviation increases towards the outer surface of the sample, which is to be expected since the laser will be turning off and on in this zone at the start and end of the scan vectors. The smaller field of view offered by photodiode 1 is likely the cause for the improved separation of the bulk hatching when compared to photodiode 1 since less surrounding material is captured by the sensor.

The remaining voxels in the range of 0.45-1.00 capture the regions of higher normalised standard deviation. In these regions, the laser is switching on and off, and travelling between the sample and its origin. This data is shown in Figure 7(c). Figure 7(c) highlights the same 4 cluster regions as the range captured from photodiode 1, including the two clusters of pores, as well as the zones where the laser is changing

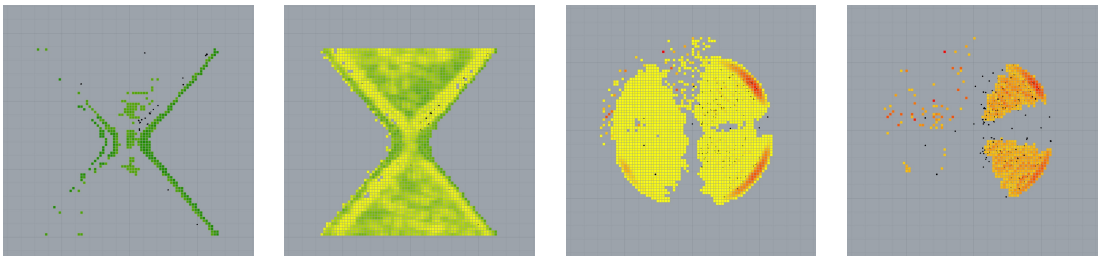

STD: 0.10-0.20 (a) | STD: 0.20-0.45 (b) | STD: 0.45-1.00 (c) | STD: 0.65-1.00 (d)

Figure 7: Images showing 2mm slices (a & b) through the sample perpendicular to the gas flow direction, and top-down (c & d) views of the voxelised data from photodiode 2 filtered within different ranges, given below each image. The colour map goes from green (low normalised standard deviation) to red (high normalised standard deviation).

direction between vectors.

The most interesting range from photodiode 2 is from 0.65-1.00 normalised standard deviation, as this encapsulates the pores from the CT scan well while excluding the rest of the part. The narrower field of view from photodiode 2 means that less data from the surrounding material is captured, and this is the likely cause for the histogram in Figure 5(b) showing a smaller spread of data through the voxels, as well as the porous regions being better defined from photodiode 2 compared to photodiode 1.

4 Concluding remarks

This work presents a pipeline for processing data collected during an LPBF build into an efficient format, permitting the calculation of spatial statistics that show a promising correlation to pores extracted from a CT scan of a printed sample. The results from this pipeline and subsequent filtering show a good spatial correlation between the standard deviation of photodiode data contained within a voxel and the porosity extracted from the CT scan.

- The proposed voxelisation step enables easy calculation of spatial statistics for the photodiode data within discrete regions of space.
- After voxelisation of the photodiode samples, the normalised standard deviation within the voxels proves to be a useful indicator of porosity in that general region.
- This normalised standard deviation acts as an indicator of the stability of the melting process within the voxels.

- Photodiode 2 better separates the defect regions from the rest of the bulk part compared to photodiode 1 and is therefore a more useful sensor for this material and processing route in predicting the appearance of defects.

The remaining pores that do not correlate with the normalised standard deviation of the voxelised data are likely caused by other stochastic effects that occur during the manufacturing process. Further investigation is needed to determine if these single random pores can be identified in the photodiode data using the proposed technique.

The authors accept that many different sources contribute to the formation of defects in the LPBF process and in this paper, only one of those has been highlighted for a single geometry. In future work, different samples containing different defect triggers will be printed and analysed to determine how well the spatial standard deviation metric predicts the formation of defects.

Acknowledgements

This project has received funding from the European Union's Horizon 2020 research and innovation programme under the Marie Skłodowska-Curie grant agreement No 956401.

References

[1] J. Wu, W. Wang, X. Gao, "Design and optimization of conforming lattice structures", IEEE Transactions on Visualization and Computer Graphics, 27, 43-56, 2021.

[2] A. Garaigordobil, R. Ansola, E. Veguería, I. Fernandez, "Overhang constraint for topology optimization of self-supported compliant mechanisms considering additive manufacturing", CAD Computer Aided Design, 109, 33-48, 2019.

[3] A. D. Plessis, I. Yadroitsev, I. Yadroitsava, S. G. L. Roux, "X-ray microcomputed tomography in additive manufacturing: A review of the current technology and applications", 3D Printing and Additive Manufacturing, 5(3), 227-247, 2018.

[4] L. Vásárhelyi, Z. Kónya, Á. Kukovecz, R. Vajtai, "Microcomputed tomography–based characterization of advanced materials: A review", Materials Today Advances, 8, 2020.

[5] J. C. Hastie, M. E. Kartal, L. N. Carter, M. M. Attallah, D. M. Mulvihill, "Classifying shape of internal pores within alsi10mg alloy manufactured by laser pow-

der bed fusion using 3d x-ray micro computed tomography: Influence of processing parameters and heat treatment", Materials Characterization, 163, 2020.

[6] S. F. Cobos, C. J. Norley, S. I. Pollmann, D. W. Holdsworth, "Cost-effective micro-ct system for non-destructive testing of titanium 3d printed medical components", PLOS ONE, 17(10), 2022.

[7] S. M. Estalaki, C. S. Lough, R. G. Landers, E. C. Kinzel, and T. Luo, "Predicting defects in laser powder bed fusion using in-situ thermal imaging data and machine learning", Additive Manufacturing, 35, 2020.

[8] Lough C, Wang X, Smith C, Landers R, Bristow D, Drallmeier J, Brown B, Kinzel E, "Correlation of SWIR imaging with LPBF 304L stainless steel part properties", Additive Manufacturing, 35, 2020.

[9] L. Yang, L. Lo, S. Ding, and T. Özel, "Monitoring and detection of meltpool and spatter regions in laser powder bed fusion of super alloy inconel 625", Progress in Additive Manufacturing, 5, 367-378, 2020.

[10] Ma H, Mao Z, Feng W, Yang Y, Hao C, Zhou J, Liu S, Xie H, Guo G, Liu Z, "Online in-situ monitoring of melt pool characteristic based on a single high-speed camera in laser powder bed fusion process", Applied Thermal Engineering, 211, 13594311, 2022.

[11] R. Drissi-Daoudi, G. Masinelli, C. de Formanoir, K. Wasmer, J. Jhabvala, and R. E. Logé, "Acoustic emission for the prediction of processing regimes in laser powder bed fusion, and the generation of processing maps", Additive Manufacturing, 67, 22148604, 2023.

[12] J. B. Forien, N. P. Calta, P. J. DePond, G. M. Guss, T. T. Roehling, M. J. Matthews, "Detecting keyhole pore defects and monitoring process signatures during laser powder bed fusion: A correlation between in situ pyrometry and ex situ x-ray radiography", Additive Manufacturing, 35, 22148604, 2020.